ACS Photonics

Article

pubs.acs.org/journal/apchd5

# Hot-Electron Dynamics and Thermalization in Small Metallic Nanoparticles

J. R. M. Saavedra,[†,‡] Ana Asenjo-Garcia,[†,‡] and F. Javier García de Abajo*[,†,§]

[†]ICFO-Institut de Ciencies Fotoniques, The Barcelona Institute of Science and Technology, 08860 Castelldefels (Barcelona), Spain
[§]ICREA-Institució Catalana de Recerca i Estudis Avançats, Passeig Lluís Companys 23, 08010 Barcelona, Spain

Supporting Information

**ABSTRACT:** The important role played by hot electrons in photocatalysis and light harvesting has attracted great interest in their dynamics and mechanisms of generation. Here, we theoretically study the temporal evolution of optically excited conduction electrons in small plasmon-supporting gold and silver nanoparticles. We describe the electron dynamics through a master equation incorporating transition rates for optical excitations and electron−electron collisions that are calculated using the screened interaction within an independent-electron picture. Upon optical excitation of the particle by a light pulse, a nonthermal electron distribution is produced, which takes 10s fs to thermalize at an elevated electron temperature due to electron−electron collisions and eventually relaxes back to ambient temperature via coupling to phonons and thermal diffusion. Phonons and diffusion are introduced through a phenomenological inelastic attenuation rate. We find the temporal evolution of the electron energy distribution to strongly depend on the total absorbed energy, which is in turn determined by particle size, pulse fluence, and photon energy. Our results provide detailed insight into hot-electron dynamics that can be beneficial for the design of improved photocatalysis and photodetection devices.

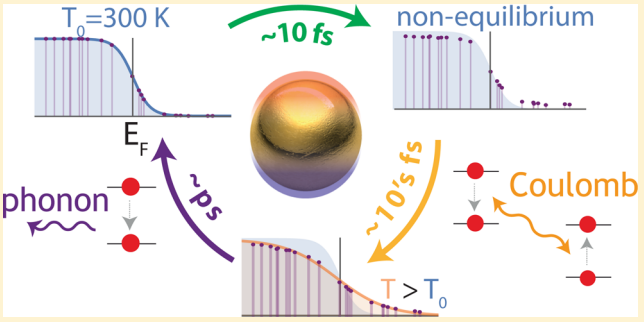


**KEYWORDS:** *hot electrons, ultrafast dynamics, nanoparticles, plasmons, electron thermalization*

The interaction of light with electrons in matter is the underlying principle of fundamental processes such as photoemission and photocatalysis. Progress in the understanding of these phenomena is generating important technological applications, for example, in optical sensing,[1−6] photochemistry,[7−11] and light harvesting.[9,12−16] In this context, metallic nanostructures provide the means to confine and enhance the electromagnetic optical field down to small regions compared to the wavelength, thus allowing us to control and increase the interaction of light with the electrons of those structures.[17,18] An important part of this interaction concerns the Landau damping mechanism of plasmon decay, which can lead to the promotion of conduction electrons to energies well above the Fermi level.[7−9,11,14,19−29] In fact, this is the main channel of plasmon damping in small metal particles, where radiative decay is negligible.

The so-called hot-electrons (and holes) can have sufficient energy to trigger chemical reactions,[7−11,27,30,31] harvest light energy,[9,12−16] induce nonlinear response,[32] and serve as photodetection signals.[22,24,33] This great potential of hot electrons for technological applications has stimulated substantial efforts to understand their dynamics, including ultrafast optical pump−probe experiments of the response of thin films[34,35] and metal nanoparticles.[36−40] The mean free path between inelastic collisions of hot-electrons in metals has been extensively examined as well.[34,41−44] Likewise, much work has been devoted to the theoretical understanding of the creation and relaxation of hot electrons.[27,28,45−53] The complexity of the problem limits the applicability of first-principles simulations to the bulk.[28,52,53] Simple analytical calculations of the cascade process have been also reported, mainly aiming a qualitative understanding.[19,20,50] A simple, detailed description of hot-electron dynamics including finite-size effects is however missing.

Here, we theoretically describe the excitation by a laser pulse and subsequent evolution of conduction electrons in small gold and silver nanoparticles, incorporating detailed information on electron−electron collision rates, which are calculated from the screened interaction. The dependence on particle size, laser intensity, and light frequency is thoroughly studied. Figure 1 presents a cartoon of the processes under consideration, which we describe through a simple master rate equation for the conduction electrons, incorporating the noted initial laser-pulse excitation, as well as e-e thermalization and relaxation through inelastic collisions.

## THEORETICAL MODEL

We consider a gold or silver nanosphere and focus on the dynamics of s conduction electrons, which we describe as

**Received:** March 28, 2016
**Published:** July 5, 2016





DOI: 10.1021/acsphotonics.6b00217
*ACS Photonics* 2016, 3, 1637−1646

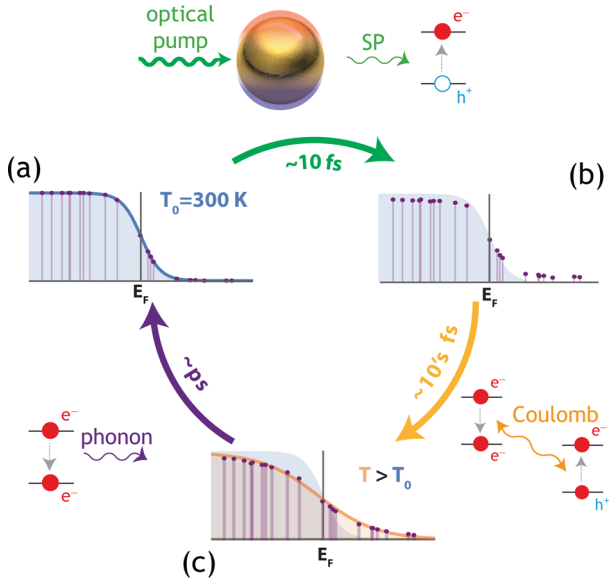


**Figure 1.** Sketch of the physical processes under consideration. (a) A gold or silver particle is initially in thermal equilibrium with its host background at temperature $T_0$. (b) An ultrafast laser pulse irradiates the particle, generating surface plasmons, which rapidly decay into hot electrons and holes within ~10 fs. (c) These charge carriers evolve due to their Coulomb interaction, leading to the decay of the most energetic electrons within 10s fs, and eventually relaxing back to ambient temperature via coupling to particle phonons within several picoseconds. Shaded areas represent the initial Fermi–Dirac distribution (FDD) of electronic states, vertical lines and symbols indicate the occupancies of different energy levels, and the solid curve in (c) is the FDD at a higher temperature $T$, as calculated for a silver particle containing $N = 10^4$ conduction electrons (see below).

independent and confined by an infinite potential well of the same diameter as the particle. The resulting wave function $\psi_i$ for each one-electron state $i$ is a simple product of a spherical Bessel function and a spherical harmonic (see Methods). Each metal atom contributes with one electron to the conduction band, so there is an unambiguous relation between the well diameter $D$ and the number of s electrons $N$. For the moderate photon energies under consideration, we neglect the dynamics of d valence-band electrons, which roughly lie 2.4 eV (4 eV) below the Fermi level of gold (silver).[9] This approximation is well justified for silver, but it is questionable near the plasmon energy of gold, which partially overlaps with d band excitations. Nevertheless, the contribution of d-band electrons to dielectric screening is included in the dielectric function that mediates the interaction between hot electrons. This dielectric function describes the applied field inside the particle, which is responsible for initial absorption from the laser pulse (see below).

We represent the configuration of conduction electrons through a set of occupation fractions $p_i$, one for each state $i$. The temporal evolution of these occupancies is here studied by means of the master equation

$$\frac{\mathrm{d}p_i(t)}{\mathrm{d}t} = -\gamma^{\text{e-ph}}(p_i - p_i^0) + \sum_{j\neq i}[\gamma_{ij}^{\text{ex}}(p_j - p_i) - \gamma_{ji}^{\text{e-e}}p_i(1-p_j) + \gamma_{ij}^{\text{e-e}}p_j(1-p_i)] \quad (1)$$

where the $\gamma$ coefficients describe transition rates associated with different physical processes. In particular, external pump (ex) and electron–electron (e-e) transitions (second term in eq 1) are weighted by appropriate combinations of occupation fractions in order to guarantee that they occur between occupied and unoccupied states. Moreover, the optical pump can produce both population and depopulation of each electron state, which are combined in a weighting factor $p_j - p_i$, exploiting the symmetry $\gamma_{ij}^{\text{ex}} = \gamma_{ji}^{\text{ex}}$ (see eq 13 in Methods). Additionally, relaxation through electron–phonon (e-ph) interaction (first term in eq 1) simply drives the system back to its initial occupancies $p_i^0 = f_i(T_0)$, where $f_i(T_0)$ is the Fermi–Dirac distribution (FDD) at the environment temperature $T = T_0$. More precisely,

$$f_i(T) = \frac{1}{e^{(E_i-\mu(T))/k_\mathrm{B}T} + 1} \quad (2)$$

where $\mu(T)$ is the temperature-dependent chemical potential (see below).

Several approximations are made for each of the three different types of processes considered in eq 1 and, more precisely, in the calculation of their associated transition rates, as we describe next:

- *Hot carrier generation through optical pump*, $\gamma_{ji}^{\text{ex}}$. We consider the particle to be irradiated by a laser pulse of fixed duration $\Delta = 10$ fs. The resulting electron excitations are described through time-dependent rates $\gamma_{ji}^{\text{ex}}$ between states $i$ and $j$. We approximate these rates by calculating the first-order transition probability produced by the laser field, conveniently corrected to include the response of the particle (i.e., the transition is driven by the field inside the particle instead of the bare incident field). For simplicity, we assimilate the particle response to that of a homogeneous sphere described in terms of a size-corrected dielectric function (see below). Finally, we derive a rate from the transition probability by assuming a normalized temporal profile that follows the pulse intensity (see eq 13 in Methods). Incidentally, the pulse fluence is simply given by $\sqrt{\pi} I_0 \Delta$ in terms of the peak light intensity $I_0$.
- *Thermalization through electron–electron interaction*, $\gamma_{ji}^{\text{e-e}}$. The screened Coulomb interaction between hot charge carriers produces $i \rightarrow j$ transitions, which we study by assuming linear response and ignoring the contribution of the transitioning electron to dielectric screening in the system (many-electron limit). A direct extension of a previously reported formula for the transition rate[52,54−56] allows us to include temperature effects and write it as

$$\gamma_{ji}^{\text{e-e}} = \frac{2e^2}{\hbar}\int \mathrm{d}\mathbf{r}\mathrm{d}\mathbf{r}'\psi_j(\mathbf{r})\psi_i^*(\mathbf{r})\psi_j^*(\mathbf{r}')\psi_i(\mathbf{r}')\mathrm{Im}\{-W(\mathbf{r},\mathbf{r}',|\omega_{ij}|)\} \times [n_\mathrm{T}(|\omega_{ij}|) + \theta(\omega_{ij})] \quad (3)$$

  where $W(\mathbf{r},\mathbf{r}',\omega)$ is the screened interaction, defined as the potential produced at $\mathbf{r}$ by a unit point charge placed at $\mathbf{r}'$ and oscillating with frequency $\omega$. Here, $n_\mathrm{T}(\omega) = [e^{\hbar\omega/k_\mathrm{B}T} - 1]^{-1}$ is the Bose–Einstein distribution function at temperature $T$, $\omega_{ij} = (E_i - E_j)/\hbar$ is the transition frequency, and the step function $\theta(\omega_{ij})$ only contributes for $E_i > E_j$. We calculate the screened interaction $W$ within the same dielectric model as the one used above for $\gamma_{ji}^{\text{ex}}$, assuming a homogeneous dielectric sphere described by a size-corrected dielectric function. This leads to analytical results for $\gamma_{ji}^{\text{e-e}}$ (see eq 14 in Methods).
- *Relaxation through electron–phonon interaction*, $\gamma^{\text{e-ph}}$. Coupling to phonons removes energy from the electrons



DOI: 10.1021/acsphotonics.6b00217
ACS Photonics 2016, 3, 1637−1646

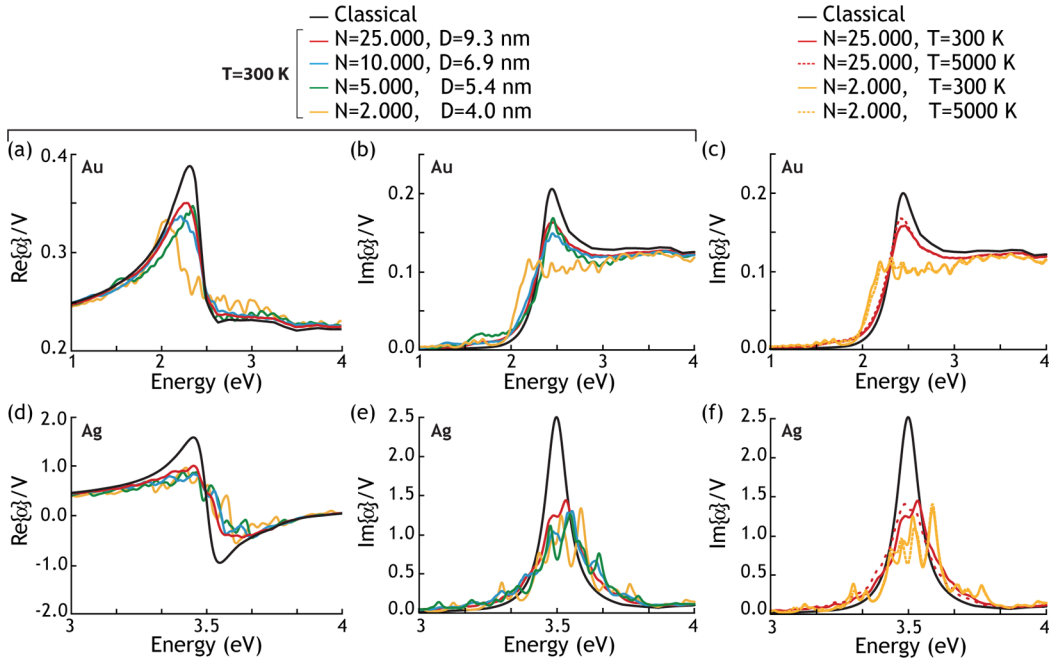


**Figure 2.** Potential-well approximation (PWA) for the dielectric function of gold and silver nanoparticles. We show the real (a, d) and imaginary (b, c, e, f) parts of the dipolar polarizability $\alpha$ calculated from the PWA (4) for gold (a–c) and silver (d–f) particles of different size (see legends for diameter $D$ and number of electrons $N$) at various electron temperatures $T$. For comparison, we also plot the classical limit $\alpha = (3V/4\pi)(\epsilon - 1)/(\epsilon + 2)$ (black curves, with the dielectric function $\epsilon$ taken from optical measurements[60]). The polarizabilities are normalized to the metal volume $V = 4\pi a^3/3$.

at a phenomenological rate $\gamma^{\text{e-ph}}$ (first term in the right-hand side of eq 1). This relaxation brings the electrons back from the current distribution $p_i$ to the initial one $p_i^0$, a process that has been extensively studied using two different temperatures for the electrons and the atomic lattice.[57−59] Instead, we incorporate a more microscopic description through $\gamma^{\text{e-ph}}$, although the effect of the increase in phonon population is disregarded in the present model, and so is thermal diffusion outside the particle. A detailed computation of the temperature-dependent $\gamma^{\text{e-ph}}$ rate is provided in Methods.

An important ingredient in the calculation of $\gamma_{ji}^{\text{ex}}$ and $\gamma_{ji}^{\text{e-e}}$ is the metal permittivity, which differs substantially from the bulk permittivity for the small particles under consideration, as we discuss next. We implement a correction that goes beyond the phenomenological description traditionally introduced through a size-dependent effective damping.[61] In particular, we construct the permittivity from the potential-well one-electron states (see eq 12 in Methods) and, therefore, we term it potential-well approximation (PWA). We first note that in a local dielectric description the electric field inside a homogeneous sphere that is exposed to a uniform external electric field is also uniform. As a reasonable ansatz, we assume a uniform field inside our metal sphere as well. Additionally, we adopt the noninteracting random-phase approximation susceptibility[62] to write the PWA for the dielectric function as[63,64]

$$\epsilon_{\text{PWA}}(\omega) = \epsilon_{\text{b}}(\omega) + \omega_{\text{p}}^2 \sum_{ij} \frac{S_{ij}}{\omega_{ij}^2 - \omega(\omega + i\gamma)} \tag{4}$$

where the sum extends over transitions between electron states $i$ and $j$, $\omega_{ij} = (E_i - E_j)/\hbar$ is the transition frequency, $\hbar\gamma = 0.071$ eV ($\hbar\gamma = 0.024$ eV) is a phenomenological damping energy derived from optical measurements for gold (silver),[60]

$$S_{ij} = \frac{2m_{\text{e}}\omega_{ij}}{\hbar N}[f_j(T) - f_i(T)]|\langle j|z|i\rangle|^2$$

is the transition strength (we consider polarization along $z$), conveniently normalized to satisfy the $f$-sum rule $\sum_{ij} S_{ij} = 1$, and $\omega_{\text{p}}$ is the classical bulk plasma frequency. The latter ($\hbar\omega_{\text{p}} = 9.0$ eV in gold and silver) depends on the particle radius $a$ and the number of conduction electrons $N$ as $\omega_{\text{p}} = \sqrt{3e^2N/m_{\text{e}}a^3}$. In eq 4 we define

$$\epsilon_{\text{b}}(\omega) = \epsilon(\omega) + \frac{\omega_{\text{p}}^2}{\omega(\omega + i\gamma)} \tag{5}$$

as a background permittivity that takes into account interband transitions and polarization of inner electrons. More precisely, $\epsilon(\omega)$ is the bulk dielectric function of the metal, which we take from optical measurements (Johnson and Christie[60] for 0.8–6.5 eV photon energies, Palik[65] above this interval, and a constant $\epsilon_{\text{b}} = 9.5$ ($\epsilon_{\text{b}} = 4$) below 0.8 eV for gold (silver)[60]). The Lorentzian in eq 5 removes the Drude contribution of conduction electrons, which is replaced by the double sum of eq 4 for the particle. Figure 2 shows the polarizability for small particles of diameters in the $D = 4$–$9.3$ nm range, calculated from the PWA as $\alpha = a^3(\epsilon_{\text{PWA}} - 1)/(\epsilon_{\text{PWA}} + 2)$. In the smallest particles under consideration, the contribution of singular electronic transitions produce fine structure, which disappears as the particle size increases, indicating a convergent trend toward the classical limit $\alpha = a^3(\epsilon - 1)/(\epsilon + 2)$. Interestingly, we observe only a minor dependence of $\epsilon_{\text{PWA}}$ on temperature (through $f_i(T)$; see Figure 2c,f), so we assume a $T$-independent permittivity throughout the rest of this work.

In what follows, we numerically solve eq 1 for different particle sizes and illumination conditions. As we are dealing



DOI: 10.1021/acsphotonics.6b00217
ACS Photonics 2016, 3, 1637−1646

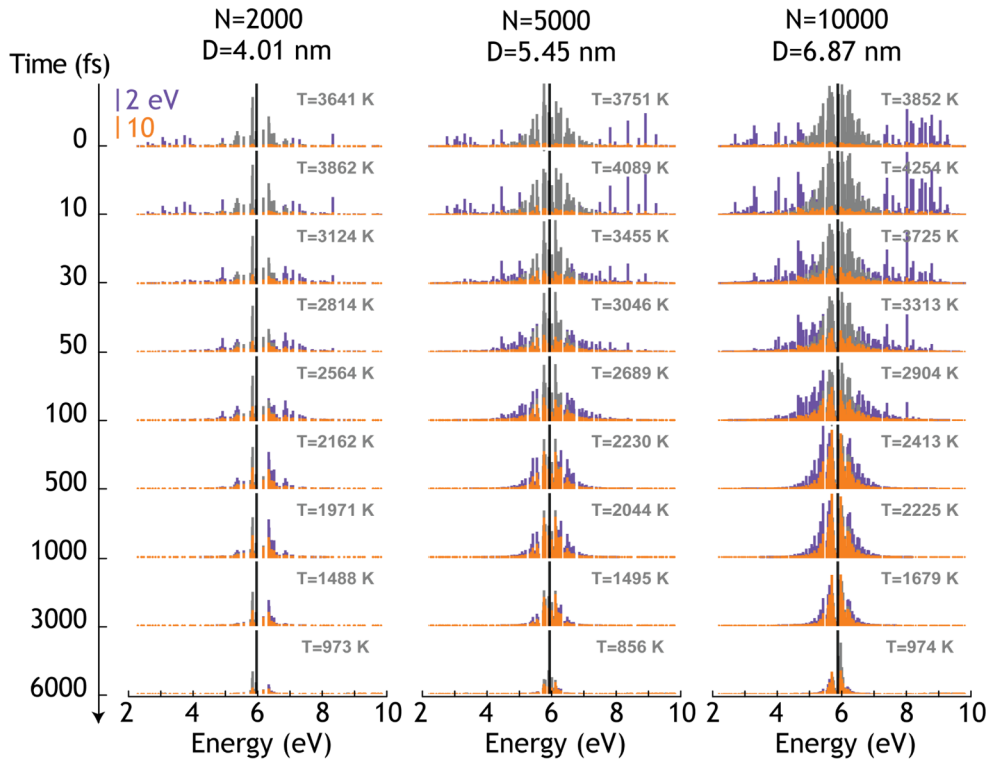


**Figure 3.** Temporal evolution of the conduction electron distribution for different Ag particle sizes. Three different diameters $D$ and corresponding numbers of conduction electrons $N$ are considered. We show the difference $|\rho_S - \rho_S^0|$ (orange lines) of the DOS (see eq 6) relative to the unperturbed particle, as well as the contribution of that difference to the electronic energy $[E_S - \mu(T_0)\,]|\rho_S - \rho_S^0|$ (purple lines), where $\mu(T_0)$ is the chemical potential at the initial ambient temperature $T_0$ = 300 K (see main text). These quantities are plotted as a function of energy $E_S$ for each set of degenerate states $S$ (horizontal axis). $\mu(T_0)$ is shown as vertical black lines. Gray lines represent FDD's at the effective temperature $T$, also indicated for each plot. The central energy, duration, and peak intensity of the light pulse are 3.5 eV, 10 fs, and $10^{14}$ W/m$^2$ (fluence equal to 0.18 mJ/cm$^2$), respectively. The central part of the pulse impinges on the particle at time 0 (upper plots).

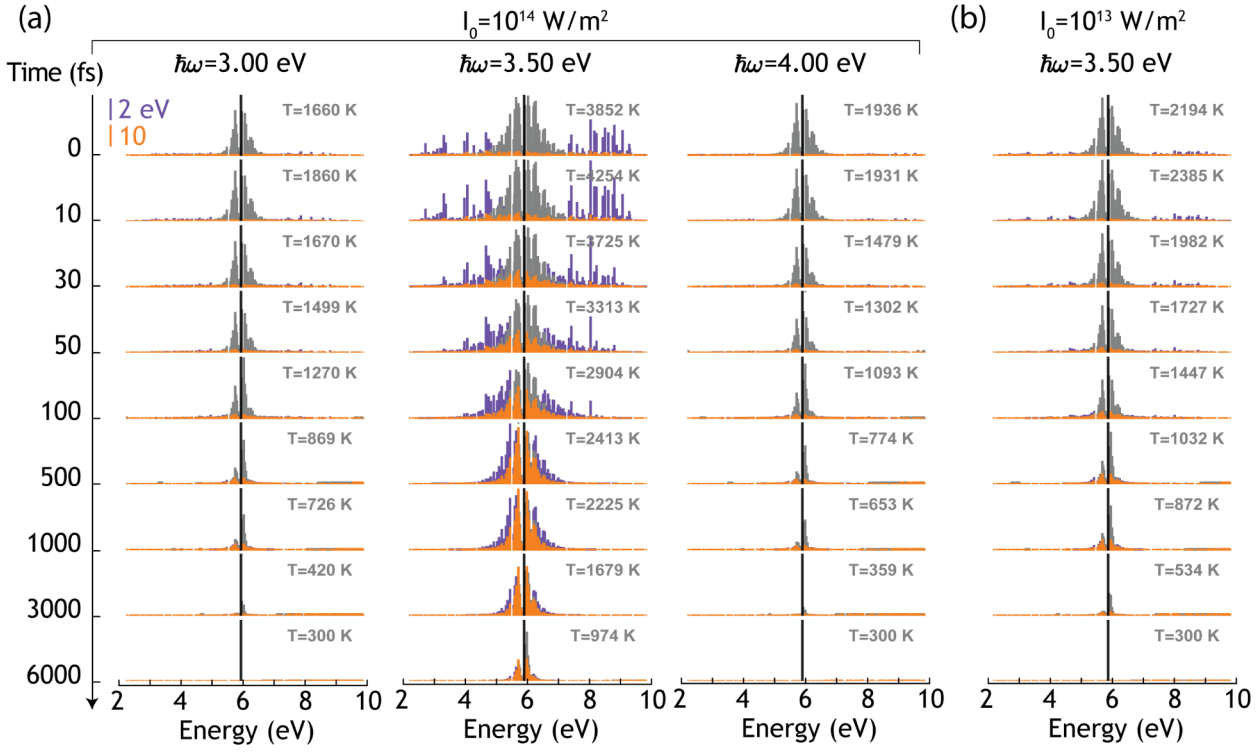


**Figure 4.** Same as Figure 3 for different values of the light pulse central energy (a) and peak intensity (b) (see labels). The particle diameter is $D$ = 6.87 nm ($N$ = $10^4$ conduction electrons).



DOI: 10.1021/acsphotonics.6b00217
ACS Photonics 2016, 3, 1637−1646

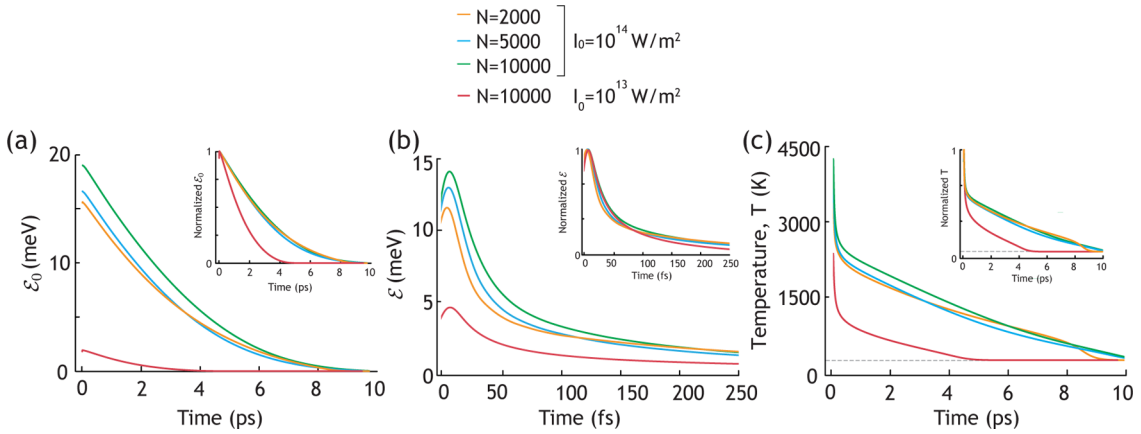


**Figure 5.** Temporal evolution of (a) the distance to initial equilibrium $\mathcal{E}_0$ (eq 7), (b) the distance to instantaneous thermal equilibrium $\mathcal{E}$ (eq 8), and (c) the electron temperature $T$ for particles of different sizes and two values of the pump peak intensity (see labels). The central energy and duration of the light pulse are 3.5 eV and 10 fs, respectively. The initial temperature is $T_0$ = 300 K. The peak of the pump pulse reaches the particle position at time 0. The insets show the same curves normalized to their respective maxima.

with a discrete system, it is convenient to define a discrete electronic density of states (DOS)

$$\rho_S = 2\sum_{i\in S} p_i \tag{6}$$

where the sum runs over subsets $S = \{\psi_i\}$ of degenerate orbitals with the same energy $E_S = E_i$, and the factor of 2 accounts for spin degeneracy. Obviously, the number of electrons $N = \sum_S \rho_S$ has to remain constant. In particular, when thermal equilibrium is established at a certain temperature $T$, we have $p_i = f_i(T)$ (see eq 2). This results in the condition $N = 2\sum_i f_i$, which allows us to determined the chemical potential $\mu(T)$ in order to maintain $N$ constant (see Methods).

We note that the particle temperature is only well-defined when the system is thermalized. However, the electron distribution is far from thermal equilibrium during the first stages following pulse irradiation. Then, we define an effective temperature determined by the condition that the electronic energy is conserved due to e-e collisions (see Methods for more details). Obviously, the effective temperature agrees with the standard value when the electron distribution approaches a FDD.

## PARTICLE SIZE DEPENDENCE OF ELECTRON THERMALIZATION

Figure 3 shows the time evolution of the electron population in silver particles following the excitation with a 10 fs laser pulse of $10^{14}$W/m$^2$ peak intensity (fluence equal to 0.18 mJ/cm$^2$) centered around 3.5 eV photon energy, which overlaps with the prominent dipole plasmon observed in silver particles for the three different sizes under consideration. The distribution right after pumping exhibits perturbations that are roughly centered around the chemical potential of the relaxed particle (we find $\mu(T_0)$ = 5.87 eV at $T_0$ = 300 K), which compares well with the well-known Fermi energies of s electrons in bulk gold and silver (5.53 and 5.49 eV, respectively[66]). The initial distribution evolves very rapidly during the first tens of femtoseconds due to e-e collisions, which produce a migration of the population perturbations toward the chemical potential, eventually thermalizing after a time >10s fs following pulse irradiation (cf. purple and gray bars in Figure 3). Finally, the electron temperature decreases at a low pace via relaxation to phonons.[67]

The effects of electron quantization are more clearly discernible in the smallest particle under consideration ($D$ = 4.01 nm), although the excited population right after irradiation does not follow a distinct pattern. In contrast, the largest particle ($D$ = 6.87 nm) roughly shows an initial excited population with features that are symmetrically placed at an energy ∼3.5 eV (the light energy) away from the chemical potential. The increase in initial excited population with particle size presumably originates in the stronger dipole moments associated with the transitions between orbitals of larger spatial extension. The perturbations remain stronger in larger particles even after a time of several picoseconds following pulse irradiation.

In Figure 4, we explore the dependence on laser pulse parameters for a $D$ = 6.87 nm particle. It is clear that by tuning the light frequency to the plasmon resonance, the carriers are maximally excited (Figure 4a). When moving to lower intensities (Figure 4b), the initial distribution remains qualitatively the same, although the perturbations are obviously smaller in magnitude. However, the relative importance of e-e thermalization and inelastic relaxation depends on electron temperature, thus leading to a comparatively faster depletion of hot electrons for lower pulse fluence.

In order to quantify the displacement of the electron distribution from the initial relaxed state of the particle, we introduce the distance to initial equilibrium

$$\mathcal{E}_0 = \frac{1}{N}\sum_S |E_S - \mu(T_0)||\rho_S - \rho_S^0| \tag{7}$$

which roughly represents the excess energy (normalized per conduction electron) remaining in the electronic system. We additionally define the distance to instantaneous thermal equilibrium

$$\mathcal{E} = \frac{1}{N}\sum_S |E_S - \mu(T)||\rho_S - 2\sum_{i\in S} f_i(T)| \tag{8}$$

where the energy and DOS are compared to the equilibrium chemical potential and state occupancies corresponding to the effective temperature $T$, which is in turn a function of time. Figure 5 shows the temporal evolution of these quantities for


DOI: 10.1021/acsphotonics.6b00217
ACS Photonics 2016, 3, 1637−1646

the same three particle sizes as in Figure 3. In particular, $T$ rises rapidly when the pump pulse illuminates the particle, and decreases slowly back to ambient temperature over a scale of several picoseconds. Interestingly, the peak value of $T$ right after irradiation is rather independent of particle size, and so is its temporal evolution. However, a strong dependence on pump intensity is observed. The evolution of $\mathcal{E}_0$ (Figure 5a) also shows an expected jump during pulse irradiation, followed by a slow decay, which in our model is entirely due to e-ph inelastic relaxation because e-e collisions conserve energy. Eventually, $\mathcal{E}_0$ becomes negligible after ~10 ps. In contrast, the distance to instantaneous equilibrium $\mathcal{E}$ (Figure 5b) rapidly decays over a time scale of 10s fs, compatible with the observed distributions of populations in Figures 3 and 4.

We remark that the temporal evolutions of $\mathcal{E}_0$, $\mathcal{E}$, and $T$ follow profiles that are rather independent of particle size when they are normalized to their maximum (see insets to Figure 5), and thus, they seem to be controlled by bulk properties already for the particle sizes under consideration. Additionally, the evolution of the normalized $\mathcal{E}$ (inset to Figure 5b) during the first 10s fs is independent of pulse energy, so we conclude that thermalization is controlled by intrinsic e-e scattering properties, rather than particle size and pulse energy. In contrast, relaxation, which occurs over a period of several picoseconds, takes comparatively longer time for lower pulse fluence, an effect that we attribute to the increase in $\gamma^{\text{e-ph}}$ with electron energy: more intense pulses produce higher temperatures, which are in turn associated with larger populations of high-energy electron states and faster coupling to phonons (see Methods). Incidentally, the sudden drop in temperature right after pulse irradiation is presumably the effect of non-equilibrium dynamics during the period in which $T$ acts as an effective parameter used to preserve energy conservation (see above).

## ELECTRON–ELECTRON COLLISION LIFETIME

The role of e-e interaction in hot-electron dynamics can be further understood by examining the corresponding lifetimes of specific excited charge carriers. For simplicity, we perform this analysis in the relaxed system. The lifetime is then obtained as

$$1/\tau_i^{\text{e-e}} = \sum_j \gamma_{ji}^{\text{e-e}}(1 - f_j) \tag{9}$$

for electrons and

$$1/\tau_i^{\text{e-e}} = \sum_j \gamma_{ij}^{\text{e-e}} f_j \tag{10}$$

for holes, where the rates $\gamma_{ji}^{\text{e-e}}$ are calculated at $T = T_0$ (see eq 3). Figure 6 shows the results for different particle sizes as a function of state energy $E = E_i$. The lifetime is similar for both electrons and holes, and diverges near the chemical potential because of the vanishing of the number of final states that they can decay into. Clearly, e-e scattering dominates the temporal dynamics of excited carriers at short times, when hot electrons have relatively large energies for which $\tau_i^{\text{e-e}}$ is in the range of a few femtoseconds. Remarkably, the lifetimes are nearly independent of particle size, in excellent agreement with the conclusions extracted from Figure 5. Our results compare reasonably well with ab initio calculations[53] (see curves in Figure 6), except at low carrier energies, where the latter incorporate e-ph interactions, which indeed dominate the lifetime for carrier energies <1 eV relative to the chemical

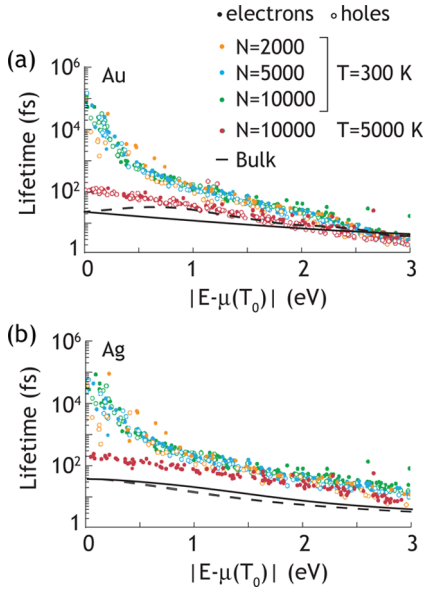


**Figure 6.** Electron–electron scattering contribution to the lifetime of electrons ($E > \mu(T_0)$, eq 9, solid circles) and holes ($E < \mu(T_0)$, eq 10, open circles) as a function of their energy $E$ relative to the initial chemical potential $\mu(T_0)$ for gold (a) and silver (b) particles of different sizes. We take $T_0$ = 300 K. Results from ab initio calculations for bulk materials taken from ref 53 are plotted for comparison as solid and dashed curves for electrons and holes.

potential. We thus expect the long-time evolution to incorporate an interplay between e-e and e-ph interactions, as a crossover between the two mechanisms occurs when electrons are eventually relaxed and piling up at lower energies (see next).

Incidentally, we also plot in Figure 6 results for a $N$ = 10 000 particle in equilibrium at a higher temperature $T$ = 5000 K, obtained by calculating both the e-e rates and the $f$'s at that temperature. The lifetime is then dramatically reduced, particularly at low energies, as a result of the increase in the number of unoccupied states that become available for electronic transitions in the charge-carrier distribution at this elevated temperature.

## COLLECTIVE RELAXATION TIME (CRT)

The population $p_i$ of a given electronic state $i$ is initially modified by the optical pump and subsequently depleted by the effect of e-e and e-ph interactions. However, the temporal evolution of these processes involves an interplay between depopulation due to transitions to other states and population by transitions from other states. The balance between these two types of processes leads to a characteristic time needed for the population $p_i$ to be substantially reduced with respect to the value right after pulse irradiation. We denote the latter $p_i^1$ and define the state-dependent CRT as the interval $\tau_i^{\text{CRT}}$ after pulse irradiation for which the difference between the state population $p_i$ and the ambient-temperature population $p_i^0$ drops to only 37% (i.e., a factor $1/e$) of its maximum value right after pulse irradiation. That is,

$$\left|p_i(\tau_i^{\text{CRT}}) - p_i^0\right| = \frac{1}{e}\left|p_i^1 - p_i^0\right| \tag{11}$$

More precisely, we consider a $\delta$-function pulse (i.e., $\Delta$ = 0), which allows us to write $p_i^1 = p_i(0^+)$. Notice that $\tau_i^{\text{CRT}}$ is expected to be much larger than the inelastic lifetime of


DOI: 10.1021/acsphotonics.6b00217
ACS Photonics 2016, 3, 1637–1646

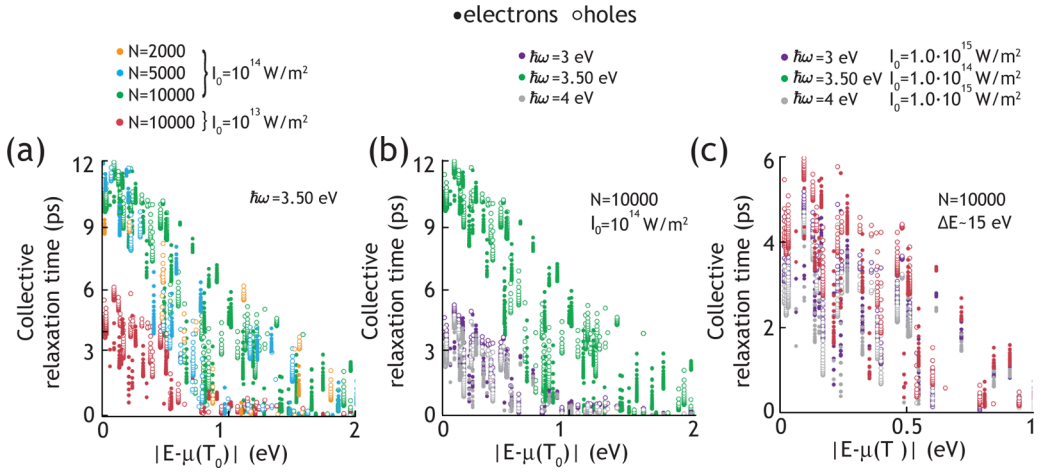


**Figure 7.** Collective relaxation time (CRT, see eq 11) of excited electrons and holes under optical pumping as a function of their energy for (a) different particle sizes and intensities with fixed central pulse energy ($\hbar\omega$ = 3.5 eV, see legend); and (b, c) different light energies and fixed particle size ($D$ = 6.87 nm, $N$ = $10^4$) with either fixed intensity ((b), $I_0$ = $10^{14}$ W/m$^2$, fluence equal to 0.18 mJ/cm$^2$) or fixed absorbed energy ((c), $\Delta E$ = 15 eV). The CRT is defined as the interval after light pulse irradiation required for the population of carriers at energy $E$ to differ from the initial population by less than 37% (i.e., a factor $1/e$) of the state degeneracy at that energy. Electrons (holes) are represented by solid (open) circles.

individual electrons (~9 fs (~31 fs) in gold (silver), as estimated from the damping rate in the infrared conductivity fitted to a Drude model[60]). In this analysis, we disregard states that are unaffected by the optical pulse due to selection rules in the initial excitation process. Figure 7 shows $\tau_i^{CRT}$ for both electrons and holes as a function of $E_i$ relative to the chemical potential. The CRT decays as the energy departs from the chemical potential $\mu$: excited electrons decay to lower-energy states, thus sustaining the population of the latter during a longer time period; the same argument applies for deeper holes; additionally, charge carriers near $\mu$ have a smaller number of states to which they can decay. A variation with pulse intensity and photon energy is clearly observed (Figure 7a,b), which is roughly explained by the difference in optically absorbed energy, as corroborated upon inspection of the CRT for pulses of different photon energy but in which the intensity is normalized in such as way that the absorbed energy is fixed (Figure 7c).

## CONCLUDING REMARKS

Our study of the dynamics of hot carriers in small metal nanoparticles corroborates the three periods of evolution illustrated by Figure 1, encompassing initial excitation by an optical pulse, fast thermalization to elevated electron temperatures over 10s fs due to e-e collisions, and subsequent relaxation back to ambient temperature over a period of several picoseconds.

The above simulations are focused on silver particles, for which the excitation of d valence electrons can be neglected at the photon energies under consideration, and in particular at the plasmon energy ~3.5 eV. We obtain qualitatively similar results for gold (see Supporting Information), although the applicability of our model to this metal is questionable for photon energies near the plasmon ~2.5 eV, which partially overlaps with d band excitations in the material. Incidentally, this is well-known to produce larger plasmon damping, which in turn leads to weaker excitation compared to silver, therefore reaching smaller peak electron temperatures.

We note that surface states are not present in our description of conduction electrons confined by a potential well. In practice, surface states strongly depend on atomic orientation,[68] which varies along the surface of an approximately round metal nanoparticle. The contribution of surface states to hot electron dynamics should then be largely dependent on the specific atomic arrangement at the surface. Furthermore, we expect this contribution to be comparatively small because surface electrons only make a small fraction of the total conduction electrons for the particle sizes under consideration.

The dynamics here investigated could be experimentally observed by employing pump−probe setups with femtosecond resolution.[69,70] For example, two-photon photoemission measurements could be used to study electron populations near the surface of metal nanoparticles. The present formalism can be easily extended to nonspherical particles in order to study shape effects on the hot electrons[37] and optimize their characteristics to suite specific applications. In particular, knowledge of the temporal evolution of hot electrons and their dependence on size, composition, and morphology in metal nanoparticles is of primary importance for the developmeng of applications in photovoltaics, photodetection, and photocatalysis.

## METHODS

**Electronic States.** We approximate the wave functions of s electrons in gold or silver spherical nanoparticles by the well-known solutions of Schrödinger equation for a spherical infinite-potential well with the same radius $a$ as the particle,

$$\psi_i(\mathbf{r}) = A_i j_{l_i}(\beta_{n_i l_i} r/a) Y_{l_i m_i}(\Omega_{\mathbf{r}}) \tag{12}$$

where $n_i$, $l_i$, and $m_i$ are the principal, orbital, and azimuthal quantum numbers, respectively, subject to the conditions $0 \le |m_i| \le l_i$, $Y_{l_i m_i}$ is a spherical harmonic, $\beta_{n_i l_i}$ is the $n_i^{th}$ zero of the spherical Bessel function $j_{l_i}$, and $A_i = \sqrt{2/[a^3 j^2_{l_i+1}(\beta_{n_i l_i})]}$ is a normalization constant. The electron energies $E_i = \hbar^2\beta^2_{n_i l_i}/(2m_e a^2)$ form a discrete spectrum with $2(2l_i + 1)$ degeneracy for each value of $n_i$, where the leading factor of 2 originates in spin.

**Excitation by a Laser Pulse.** We model the pulse through the external potential



DOI: 10.1021/acsphotonics.6b00217
ACS Photonics 2016, 3, 1637−1646

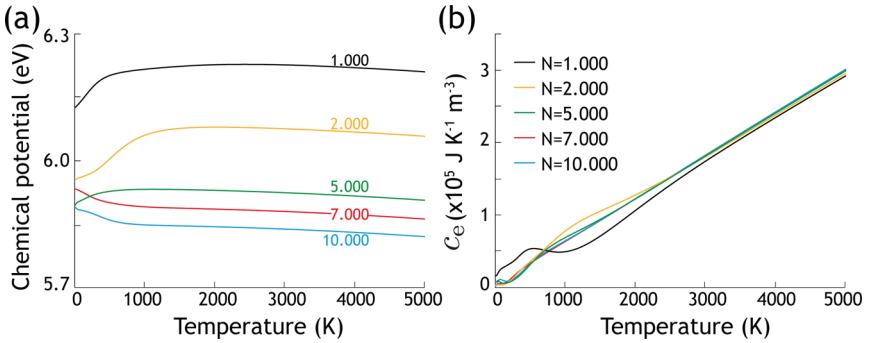


**Figure 8.** Temperature dependence of (a) the chemical potential and (b) the electronic specific heat for particles with different numbers of conduction electrons $N$ (see legends).

$$\phi^{\text{ext}}(\mathbf{r}, t) = -zE_0[e^{-i\omega_0 t}e^{-t^2/2\Delta^2} + \text{c.c.}]$$

where $\Delta$ is the duration, $\omega_0$ is the central frequency, and the peak intensity is related to the field amplitude as $I_0 = c|E_0|^2/2\pi$. It is convenient to express $\phi^{\text{ext}}$ in frequency space, so that the total potential $\phi$ inside the sphere is simply obtained by multiplying by $3/[\epsilon_{\text{PWA}}(\omega) + 2]$,[71] where we assume that the particle responds as a homogeneous sphere of permittivity $\epsilon_{\text{PWA}}$ (see eq 4). Moving back to the time domain, we find

$$\phi(\mathbf{r}, t) = -\sqrt{2\pi}zE_0\Delta \int \frac{d\omega}{2\pi} e^{-i\omega t} \frac{3F(\omega)}{\epsilon_{\text{PWA}}(\omega) + 2}$$

where $F(\omega) = e^{-(\omega-\omega_0)^2\Delta^2/2} + e^{-(\omega+\omega_0)^2\Delta^2/2}$. Transitions between conduction electrons are then described by the interaction Hamiltonian $-e\phi$. Within first-order perturbation theory, we readily find the transition probability from state $\psi_i$ to state $\psi_j$ as

$$P_{ji}^{\text{ex}} = \frac{24\pi^2 e^2 |E_0|^2 \Delta^2 a^8}{\hbar^2 |\epsilon_{\text{PWA}}(\omega_{ji}) + 2|^2} A_j^2 A_i^2 R_{ij,3}^2 M_{ji,10}^2 F^2(\omega_{ji})$$

where $\omega_{ji} = (E_j - E_i)/\hbar$ is the transition frequency and we use the radial and angular matrix elements $R_{ji,n} = \int_0^1 x^n \mathrm{d}x j_{l_i}(\beta_{n,l_i}x) j_{l_j}(\beta_{n,l_j}x)$ and $M_{ji,lm} = \int \mathrm{d}\Omega_{\mathbf{r}} Y_{l_j m_j}^*(\Omega_{\mathbf{r}}) Y_{lm}(\Omega_{\mathbf{r}}) Y_{l_i m_i}(\Omega_{\mathbf{r}})$, respectively. The Gaunt integrals $M_{ji,lm}$ can be analytically evaluated in terms of Wigner 3$j$ symbols. Finally, we distribute the probability over a time-dependent rate (i.e., the quantity actually entering eq 1)

$$\gamma_{ji}^{\text{ex}}(t) = \frac{1}{\sqrt{\pi}\Delta} e^{-t^2/\Delta^2} P_{ji}^{\text{ex}} \tag{13}$$

with the same profile as the pulse intensity.

**Screened Electron–Electron Interaction and Scattering Rates.** In order to evaluate the e-e scattering rates $\gamma_{ji}^{\text{e-e}}$ (see eq 3) we need to consider the screened interaction $W$, which for our metal particle, described as a homogeneous sphere of permittivity $\epsilon_{\text{PWA}}$ (see eq 4), reduces to[56]

$$W(\mathbf{r}, \mathbf{r}', \omega) = \sum_{l=0}^{\infty} \sum_{m=-l}^{m=l} \frac{4\pi}{2l+1} W_l(r, r', \omega) Y_{lm}(\Omega_{\mathbf{r}}) Y_{lm}^*(\Omega_{\mathbf{r}'})$$

where

$$W_l(r, r', \omega) = \frac{r_<^l}{r_>^{l+1}\epsilon_{\text{PWA}}(\omega)} + \left[\frac{2l+1}{l(\epsilon_{\text{PWA}}(\omega)+1)+1} - \frac{1}{\epsilon_{\text{PWA}}(\omega)}\right] \times \frac{(rr')^l}{a^{2l+1}}$$

$r_< = \min\{r,r'\}$ and $r_> = \max\{r,r'\}$. Introducing this expression in eq 3, we find

$$\gamma_{ji}^{\text{e-e}} = -\frac{8\pi e^2 a^5}{\hbar} A_i^2 A_j^2 \sum_{l=|l_i-l_j|}^{l_i+l_j} \frac{M_{ji,lm_j-m_i}^2}{2l+1} \text{Im}\{G_l\}[n_T(|\omega_{ji}|) + \theta(\omega_{ij})] \tag{14}$$

where

$$G_l = \frac{1}{\epsilon_{\text{PWA}}(|\omega_{ij}|)} \int_0^1 \mathrm{d}x j_{l_j}(\beta_{n_j l_j} x) j_{l_i}(\beta_{n_i l_i} x) g_l(x) + \left[\frac{2l+1}{l(\epsilon_{\text{PWA}}(|\omega_{ij}|)+1)+1} - \frac{1}{\epsilon_{\text{PWA}}(|\omega_{ij}|)}\right] R_{ji,2+l}^2$$

$$g_l(x) = x^{1-l} \int_0^x \mathrm{d}y y^{2+l} j_{l_j}(\beta_{n_j l_j} y) j_{l_i}(\beta_{n_i l_i} y) + x^{l+2} \int_x^1 \mathrm{d}y y^{1-l} j_{l_j}(\beta_{n_j l_j} y) j_{l_i}(\beta_{n_i l_i} y)$$

and only even $l + l_i + l_j$ terms with $|m_i - m_j| \le l$ contribute to the above sum.

**Chemical Potential and Specific Heat.** Figure 8a shows the temperature-dependence of the chemical potential $\mu$, which is the same for gold and silver within our model because both metals have a similar conduction electron density. We note that $\mu$ shows a trend toward the bulk metal value for increasing particle size (~5.5 eV, see Figure 8a). Finally, we calculate the electronic specific heat as a function of temperature $T$ from[75]

$$c_e(T) = \frac{\partial(E/V)}{\partial T} = \frac{2}{V}\frac{\partial}{\partial T}\sum_i E_i f_i(T)$$

This expression leads to the expected linear behavior for large particles (see Figure 8b). In contrast, finite-size effects produce a nonmonotonic behavior at low temperatures in small particles, which has been previously attributed to insufficient electron Coulomb screening.[72−74]

**Inelastic Relaxation.** We describe inelastic relaxation due to e-ph coupling in a phenomenological fashion through a state-independent decay rate $\gamma^{\text{e-ph}}$. The rate of change in the population $p_i$ is then given by $-\gamma^{\text{e-ph}}(p_i - p_i^0)$, where $p_i^0 = f_i(T_0)$ is the initial equilibrium distribution at the background temperature $T_0$ (see eq 2). The coupling rate is related to the heat capacity $c_e(T)$ through[76] $\gamma^{\text{e-ph}} = G/c_e(T)$, where the electron–lattice coupling coefficient is $G_{\text{Au}} \approx 3 \times 10^{16}$ W m$^{-3}$ K$^{-1}$ and $G_{\text{Ag}} \approx 3.5 \times 10^{16}$ W m$^{-3}$ K$^{-1}$ for gold and silver,[57,58] respectively (i.e., approximately constant over the range of temperatures here encountered). The inverse rate $1/\gamma^{\text{e-ph}}$ has a nearly linear behavior with temperature (i.e., proportional to the curves of Figure 8b), except for the anomalous nonmonotonic dependence in the smallest particles under consideration.

**Determination of a Time-Dependent Temperature from Energy Conservation.** The e-e scattering rates depend



DOI: 10.1021/acsphotonics.6b00217
ACS Photonics 2016, 3, 1637−1646

on temperature through the term $n_T$ in eq 3. However, a temperature cannot be properly defined during a time interval shortly after pulse irradiation, when the electron distribution is out of thermal equilibrium. We define an effective temperature $T$ determined in such a way that energy is conserved during e-e scattering. That is, $T$ is obtained at every time step during the evolution described by eq 1 by guaranteeing that the condition

$$\sum_{ij} E_i[\gamma_{ji}^{e\text{-}e} p_i(1-p_j) - \gamma_{ij}^{e\text{-}e} p_j(1-p_i)] = 0$$

is satisfied. Examples of temperatures calculated following this procedure are shown in Figure 5c.

## ■ ASSOCIATED CONTENT

### Supporting Information

The Supporting Information is available free of charge on the ACS Publications website at DOI: 10.1021/acsphotonics.6b00217.

Three supplementary figures with calculations for gold particles under similar conditions, as in Figures 3, 4, and 5, considering higher pump intensities (PDF).

## ■ AUTHOR INFORMATION


### Corresponding Author

*E-mail: javier.garciadeabajo@icfo.es.

### Author Contributions

‡These two authors contributed equally.


### Notes

The authors declare no competing financial interest.

## ■ ACKNOWLEDGMENTS

This work has been supported in part by the Spanish MINECO (MAT2014-59096-P and SEV2015-0522), Fundació privada CELLEX, and AGAUR (FI_B-00492-2015 and 2014-SGR-1400).

## ■ REFERENCES


(1) Kneipp, K.; Wang, Y.; Kneipp, H.; Perelman, L. T.; Itzkan, I.; Dasari, R. R.; Feld, M. S. Single molecule detection using surface-enhanced Raman scattering (SERS). *Phys. Rev. Lett.* **1997**, *78*, 1667−1670.

(2) Nie, S.; Emory, S. R. Probing single molecules and single nanoparticles by surface-enhanced Raman scattering. *Science* **1997**, *275*, 1102−1106.

(3) Xu, H.; Bjerneld, E. J.; Käll, M.; Börjesson, L. Spectroscopy of single hemoglobin molecules by surface enhanced Raman scattering. *Phys. Rev. Lett.* **1999**, *83*, 4357−4360.

(4) Moskovits, M. Surface-enhanced Raman spectroscopy: a brief retrospective. *J. Raman Spectrosc.* **2005**, *36*, 485−496.

(5) Anker, J. N.; Hall, W. P.; Lyandres, O.; Shah, N. C.; Zhao, J.; Van Duyne, R. P. Biosensing with plasmonic nanosensors. *Nat. Mater.* **2008**, *7*, 442−453.

(6) Rodríguez-Lorenzo, L.; Álvarez-Puebla, R. A.; Pastoriza-Santos, I.; Mazzucco, S.; Stéphan, O.; Kociak, M.; Liz-Marzán, L. M.; García de Abajo, F. J. Zeptomol detection through controlled ultrasensitive surface-enhanced Raman scattering. *J. Am. Chem. Soc.* **2009**, *131*, 4616−4618.

(7) Mukherjee, S.; Libisch, F.; Large, N.; Neumann, O.; Brown, L. V.; Cheng, J.; Lassiter, J. B.; Carter, E. A.; Nordlander, P.; Halas, N. J. Hot Electrons do the impossible: Plasmon-induced dissociation of $H_2$ on Au. *Nano Lett.* **2013**, *13*, 240−247.

(8) Baffou, G.; Quidant, R. Nanoplasmonics for Chemistry. *Chem. Soc. Rev.* **2014**, *43*, 3898−3907.

(9) Clavero, C. Plasmon-induced hot-electron generation at nanoparticle/metal-oxide interfaces for photovoltaic and photocatalytic devices. *Nat. Photonics* **2014**, *8*, 95−103.

(10) Park, J. Y.; Kim, S. M.; Lee, H.; Naik, B. Hot electron and surface plasmon-driven catalytic reaction in metal-semiconductor nanostructures. *Catal. Lett.* **2014**, *144*, 1996−2004.

(11) Moskovits, M. The case for plasmon-derived hot carrier devices. *Nat. Nanotechnol.* **2015**, *10*, 6.

(12) Atwater, H. A.; Polman, A. Plasmonics for improved photovoltaic devices. *Nat. Mater.* **2010**, *9*, 205−213.

(13) Linic, S.; Christopher, P.; Ingram, D. B. Plasmonic-metal nanostructures for efficient conversion of solar to chemical energy. *Nat. Mater.* **2011**, *10*, 911−921.

(14) Atar, F. B.; Battal, E.; Aygun, L. E.; Daglar, B.; Bayindir, M.; Okyay, A. K. Plasmonically enhanced hot electron based photovoltaic device. *Opt. Express* **2013**, *21*, 7196−7201.

(15) García de Arquer, F. P.; Mihi, A.; Konstantatos, G. Molecular interfaces for plasmonic hot electron photovoltaics. *Nanoscale* **2015**, *7*, 2281−2288.

(16) Wu, K.; Chen, J.; McBride, J. R.; Lian, T. Efficient hot-electron transfer by a plasmon-induced interfacial charge-transfer transition. *Science* **2015**, *349*, 632−635.

(17) Zia, R.; Schuller, J. A.; Chandran, A.; Brongersma, M. L. Plasmonics: The next chip-scale technology. *Mater. Today* **2006**, *9*, 20−27.

(18) Polman, A. Plasmonics applied. *Science* **2008**, *322*, 868−869.

(19) Ritchie, R. H.; Ashley, J. C. The interaction of hot electrons with a free electron gas. *J. Phys. Chem. Solids* **1965**, *26*, 1689−1694.

(20) Ritchie, R. H. Coupled electron-hole cascade in a free electron gas. *J. Appl. Phys.* **1966**, *37*, 2276−2278.

(21) Rösler, M.; Brauer, W. Theory of electron emission from nearly-free-electron metals by proton and electron bombardment. *Particle Induced Electron Emission I*; Springer-Verlag: Berlin, 1991; Vol. *122*, pp 1−65.

(22) Lee, Y. K.; Jung, C. H.; Park, J.; Seo, H.; Somorjai, G. A.; Park, J. Y. Surface plasmon-driven hot electron flow probed with metal-semiconductor nanodiodes. *Nano Lett.* **2011**, *11*, 4251−4255.

(23) Govorov, A. O.; Zhang, H.; Gun'ko, Y. K. Theory of photoinjection of hot plasmonic carriers from metal nanostructures into semiconductors and surface molecules. *J. Phys. Chem. C* **2013**, *117*, 16616−16631.

(24) Chalabi, H.; Schoen, D.; Brongersma, M. L. Hot-electron photodetection with a plasmonic nanostripe antenna. *Nano Lett.* **2014**, *14*, 1374−1380.

(25) Govorov, A. O.; Zhang, H.; Demir, H. V.; Gunḱo, Y. K. Photogeneration of hot plasmonic electrons with metal nanocrystals: Quantum description and potential applications. *Nano Today* **2014**, *9*, 85−101.

(26) Manjavacas, A.; Liu, J. G.; Kulkarni, V.; Nordlander, P. Plasmon-induced hot carriers in metallic nanoparticles. *ACS Nano* **2014**, *8*, 7630−7638.

(27) Mukherjee, S.; Zhou, L.; Goodman, A. M.; Large, N.; Ayala-Orozco, C.; Zhang, Y.; Nordlander, P.; Halas, N. J. Hot-electron-induced dissociation of $H_2$ on gold nanoparticles supported on $SiO_2$. *J. Am. Chem. Soc.* **2014**, *136*, 64−67.

(28) Sundararaman, R.; Narang, P.; Jermyn, A. S.; Goddard, W. A.; Atwater, H. A. Theoretical predictions for hot-carrier generation from surface plasmon decay. *Nat. Commun.* **2014**, *5*, 5788.

(29) Brongersma, M. L.; Halas, N. J.; Nordlander, P. Plasmon-induced hot carrier science and technology. *Nat. Nanotechnol.* **2015**, *10*, 25−34.

(30) Sil, D.; Gilroy, K. D.; Niaux, A.; Boulesbaa, A.; Neretina, S.; Borguet, E. Seeing is believing: Hot electron based gold nanoplasmonic optical hydrogen sensor. *ACS Nano* **2014**, *8*, 7755−7762.

(31) Sakamoto, H.; Ohara, T.; Yasumoto, N.; Shiraishi, Y.; Ichikawa, S.; Tanaka, S.; Hirai, T. Hot-electron-induced highly efficient $O_2$ activation by Pt nanoparticles supported on $Ta_2O_5$ driven by visible light. *J. Am. Chem. Soc.* **2015**, *137*, 9324−9332.




DOI: 10.1021/acsphotonics.6b00217
*ACS Photonics* 2016, 3, 1637−1646

(32) Naik, G. V.; Dionne, J. A. Photon upconversion with hot carriers in plasmonic systems. *Appl. Phys. Lett.* **2015**, *107*, 133902.
(33) Knight, M. W.; Sobhani, H.; Nordlander, P.; Halas, N. J. Photodetection with active optical antennas. *Science* **2011**, *332*, 702−704.
(34) Brorson, S. D.; Fujimoto, J. G.; Ippen, E. P. Femtosecond electronic heat-transport dynamics in thin gold films. *Phys. Rev. Lett.* **1987**, *59*, 1962−1965.
(35) Del Fatti, N.; Voisin, C.; Achermann, M.; Tzortzakis, S.; Christofilos, D.; Vallée, F. Nonequilibrium electron dynamics in noble metals. *Phys. Rev. B: Condens. Matter Mater. Phys.* **2000**, *61*, 16956−16966.
(36) Perner, M.; Bost, P.; Lemmer, U.; von Plessen, G.; Feldmann, J.; Becker, U.; Mennig, M.; Schmitt, M.; Schmidt, H. Optically induced damping of the surface plasmon resonance in gold colloids. *Phys. Rev. Lett.* **1997**, *78*, 2192−2195.
(37) Perner, M.; Gresillon, S.; März, J.; von Plessen, G.; Feldmann, J.; Porstendorfer, J.; Berg, K. J.; Berg, G. Observation of hot-electron pressure in the vibration dynamics of metal nanoparticles. *Phys. Rev. Lett.* **2000**, *85*, 792−795.
(38) Sönnichsen, C.; Franzl, T.; Wilk, T.; von Plessen, G.; Feldmann, J.; Wilson, O.; Mulvaney, P. Drastic reduction of plasmon damping in gold nanorods. *Phys. Rev. Lett.* **2002**, *88*, 077402.
(39) Arbouet, A.; Voisin, C.; Christofilos, D.; Langot, P.; Del Fatti, N.; Vallée, F.; Lermé, J.; Celep, G.; Cottancin, E.; Gaudry, M.; et al. Electron-phonon scattering in metal clusters. *Phys. Rev. Lett.* **2003**, *90*, 177401.
(40) Aruda, K. O.; Tagliazucchi, M.; Sweeney, C. M.; Hannah, D. C.; Schatz, G. C.; Weiss, E. A. Identification of parameters through which surface chemistry determines the lifetimes of hot electrons in small Au nanoparticles. *Proc. Natl. Acad. Sci. U. S. A.* **2013**, *110*, 4212−4217.
(41) Quinn, J. J. Range of excited electrons in metals. *Phys. Rev.* **1962**, *126*, 1453−1457.
(42) Kreibig, U.; Fragstein, C. V. The limitation of electron mean free path in small silver particles. *Eur. Phys. J. A* **1969**, *224*, 307−323.
(43) Penn, D. R. Electron mean free paths for free-electron-like materials. *Phys. Rev. B* **1976**, *13*, 5248−5254.
(44) Tanuma, S.; Powell, C. J.; Penn, D. R. Calculations of electron inelastic mean free paths. IX. Data for 41 elemental solids over the 50 eV to 30 keV range. *Surf. Interface Anal.* **2011**, *43*, 689−713.
(45) Popov, V. V.; Solodkaya, T. I.; Bagaeva, T. Y. Monte Carlo study of electron-plasmon scattering effect on hot electron transport in GaAs. *Phys. B* **1996**, *217*, 118−126.
(46) Keyling, R.; Schöne, W. D.; Ekardt, W. Comparison of the lifetime of excited electrons in noble metals. *Phys. Rev. B: Condens. Matter Mater. Phys.* **2000**, *61*, 1670−1673.
(47) Quijada, M.; Díez-Muiño, R.; Borisov, A. G.; Alonso, J. A.; Echenique, P. M. The lifetime of electronic excitations in metal clusters. *Nanotechnology* **2005**, *16*, S176−S180.
(48) Silkin, V. M.; Quijada, M.; Vergniory, M. G.; Alducin, M.; Boris, A. G.; Díez Muiño, R.; Juaristi, J. I.; Sánchez-Portal, D.; Chulkov, E. V.; Echenique, P. M. Dynamic screening and electron dynamics in low-dimensional metal systems. *Nucl. Instrum. Methods Phys. Res., Sect. B* **2007**, *258*, 72−78.
(49) Quijada, M.; Díez-Muiño, R.; Borisov, A. G.; Alonso, J. A.; Echenique, P. M. Lifetime of electronic excitations in metal nanoparticles. *New J. Phys.* **2010**, *12*, 053023.
(50) Kornbluth, M.; Nitzan, A.; Seideman, T. Light-induced electronic non-equilibrium in plasmonic particles. *J. Chem. Phys.* **2013**, *138*, 174707.
(51) Kumarasinghe, C. S.; Premaratne, M.; Bao, Q.; Agrawal, G. P. Theoretical analysis of hot electron dynamics in nanorods. *Sci. Rep.* **2015**, *5*, 12140.
(52) Bernardi, M.; Mustafa, J.; Neaton, J. B.; Louie, S. G. Theory and computation of hot carriers generated by surface plasmon polaritons in noble metals. *Nat. Commun.* **2015**, *6*, 7044.
(53) Brown, A. M.; Sundararaman, R.; Narang, P.; W, A. G., III; Atwater, H. A. Nonradiative plasmon decay and hot carrier dynamics: Effects of phonons, surfaces, and geometry. *ACS Nano* **2016**, *10*, 957−966.
(54) Echenique, P. M.; Pitarke, J. M.; Chulkov, E. V.; Rubio, A. Theory of inelastic lifetimes of low-energy electrons in metals. *Chem. Phys.* **2000**, *251*, 1−35.
(55) Echenique, P. M.; Berndt, R.; Chulkov, E. V.; Faster, T.; Goldmann, A.; Hofer, U. Decay of electronic excitations at metal surfaces. *Surf. Sci. Rep.* **2004**, *52*, 219−317.
(56) García de Abajo, F. J. Optical excitations in electron microscopy. *Rev. Mod. Phys.* **2010**, *82*, 209−275.
(57) Groenenveld, R. H. M.; Sprik, R.; Lagendijk, A. Femtosecond spectroscopy of electron-electron and electron-phonon energy relaxation in Ag and Au. *Phys. Rev. B: Condens. Matter Mater. Phys.* **1995**, *51*, 11433.
(58) Lin, Z.; Zhigilei, L. V.; Celli, V. Electron-phonon coupling and electron heat capacity of metals under conditions of strong electron-phonon nonequilibrium. *Phys. Rev. B: Condens. Matter Mater. Phys.* **2008**, *77*, 075133.
(59) Hopkins, P. E.; Bauer, M. L.; Duda, J. C.; Smoyer, J. L.; English, T. S.; Norris, P. M.; Beechem, T. E.; Stewart, D. A. Ultrafast thermoelectric properties of gold under conditions of strong electron-phonon nonequilibrium. *J. Appl. Phys.* **2010**, *108*, 104907.
(60) Johnson, P. B.; Christy, R. W. Optical constants of the noble metals. *Phys. Rev. B* **1972**, *6*, 4370−4379.
(61) Kreibig, U.; Vollmer, M. *Optical Properties of Metal Clusters*; Springer-Verlag: Berlin, 1995.
(62) Pines, D.; Nozières, P. *The Theory of Quantum Liquids*; W. A. Benjamin, Inc.: New York, 1966.
(63) Genzel, L.; Martin, T.; Kreibig, U. Dielectric function and plasma resonances of small metal particles. *Z. Phys. B: Condens. Matter Quanta* **1975**, *21*, 339−346.
(64) Kraus, W. A.; Schatz, G. C. Plasmon resonance broadening in small metal particles. *J. Chem. Phys.* **1983**, *79*, 6130.
(65) Palik, E. D. *Handbook of Optical Constants of Solids*; Academic Press: San Diego, 1985.
(66) Ashcroft, N. W.; Mermin, N. D. *Solid State Physics*; Harcourt College Publishers: New York, 1976.
(67) Sun, C.-K.; Vallée, F.; Acioli, L. H.; Ippen, E. P.; Fujimoto, J. G. Femtosecond-tunable measurement of electron thermalization in gold. *Phys. Rev. B: Condens. Matter Mater. Phys.* **1994**, *50*, 15337−15348.
(68) Chulkov, E.; Silkin, V.; Echenique, P. Image potential states on metal surfaces: binding energies and wave functions. *Surf. Sci.* **1999**, *437*, 330−352.
(69) Klar, T.; Perner, M.; Grosse, S.; von Plessen, G.; Spirkl, W.; Feldmann, J. Surface-plasmon resonances in single metallic nanoparticles. *Phys. Rev. Lett.* **1998**, *80*, 4249−4252.
(70) Föhlisch, A.; Feulner, P.; Hennies, F.; Fink, A.; Menzel, D.; Sánchez-Portal, D.; Echenique, P. M.; Wurth, W. Direct observation of electron dynamics in the attosecond domain. *Nature* **2005**, *436*, 373.
(71) Jackson, J. D. *Classical Electrodynamics*; Wiley: New York, 1999.
(72) Schmidt, M.; Kusche, R.; Hippler, T.; Donges, J.; Krönmuller, W.; von Issendorf, B.; Haberland, H. Negative heat capacity for a cluster of 147 sodium atoms. *Phys. Rev. Lett.* **2001**, *86*, 1191−1194.
(73) Grether, M.; de Llano, M.; Solis, M. A. Anomalous behavior of ideal Fermi gas below two dimensions. *Eur. Phys. J. D* **2003**, *25*, 287−291.
(74) Schmidt, F.-P.; Ditlbacher, H.; Hohenester, U.; Hohenau, A.; Hofer, F.; Krenn, J. R. Universal dispersion of surface plasmons in flat nanostructures. *Nat. Commun.* **2014**, *5*, 3604.
(75) Pathria, R. K.; Beale, P. D. *Statistical Mechanics*; Butterworth-Heinemann: Oxford, 1996.
(76) Tsiatmas, A.; Atmatzakis, E.; Papasimakis, N.; Fedotov, V.; Luk'yanchuk, B.; Zheludev, N. I.; García de Abajo, F. J. Optical generation of intense ultrashort magnetic pulses at the nanoscale. *New J. Phys.* **2013**, *15*, 113035.


DOI: 10.1021/acsphotonics.6b00217
*ACS Photonics* 2016, 3, 1637−1646

# Hot-Electron Dynamics and Thermalization in Small Metallic Nanoparticles – Supporting Information –

J. R. M. Saavedra,[1,*] Ana Asenjo-Garcia,[1,*] and F. Javier García de Abajo[1,2,†]

[1] *ICFO-Institut de Ciencies Fotoniques, The Barcelona Institute of Science and Technology, 08860 Castelldefels (Barcelona), Spain*
[2] *ICREA-Institució Catalana de Recerca i Estudis Avançats, Passeig Lluís Companys 23, 08010 Barcelona, Spain*

(Dated: July 9, 2016)

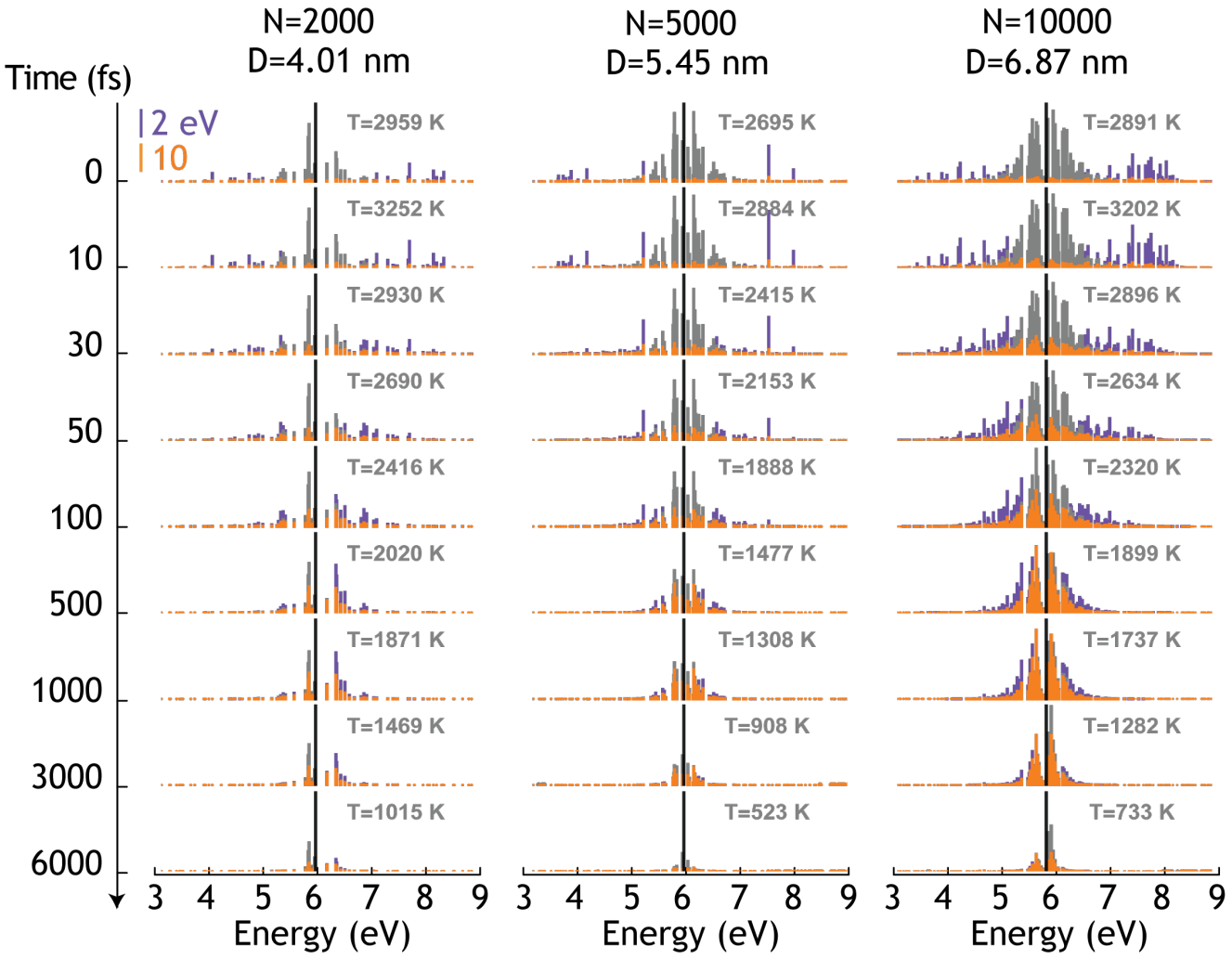


FIG. S1: Same as Fig. 3 of the main paper for gold particles, higher pump intensity ($I_0 = 10^{15}$ W/m$^2$), and central photon energy tuned to the gold-particle dipole plasmon energy (2.44 eV).

*These two authors contributed equally
†Electronic address: javier.garciadeabajo@icfo.es

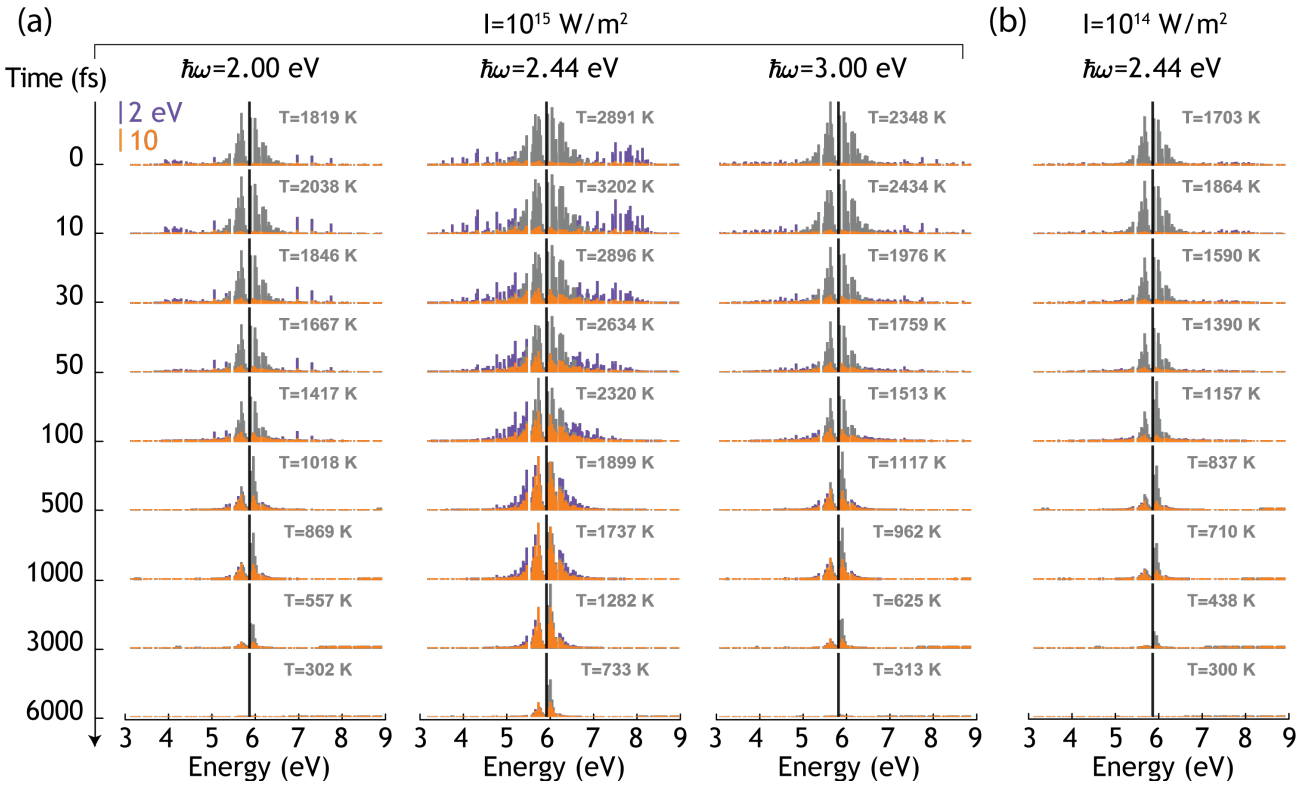


FIG. S2: Same as Fig. 4 of the main paper for gold particles, higher pump intensity, and different photon energies.

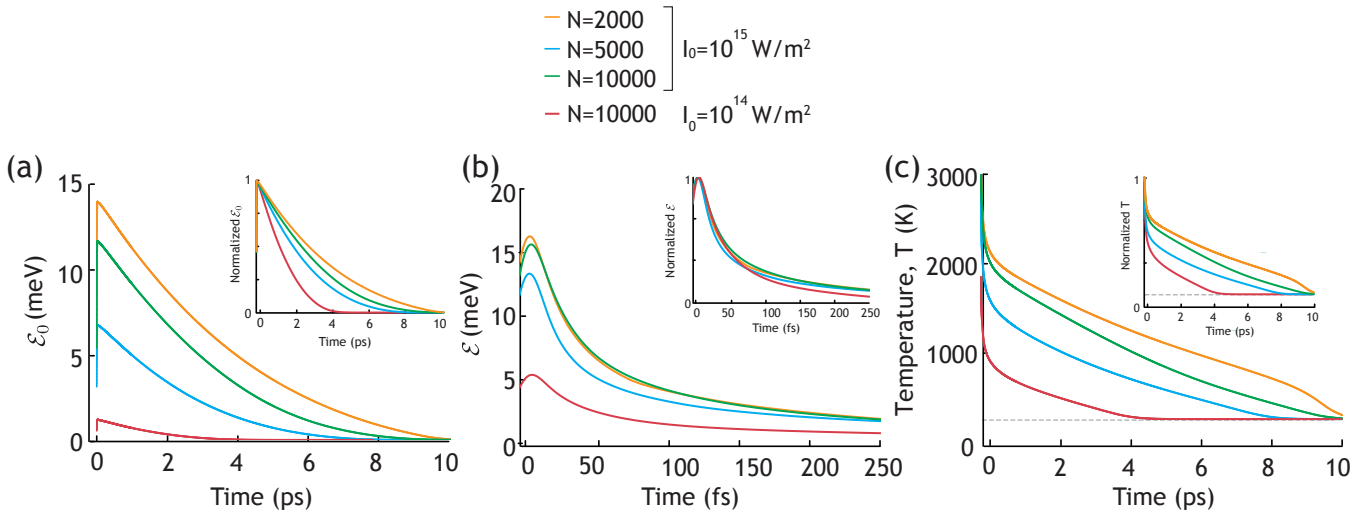


FIG. S3: Same as Fig. 5 of the main paper for gold particles, higher pump intensity, and central photon energy tuned to the gold-particle dipole plasmon energy (2.44 eV).